Quantum stress in chaotic billiards

Karl-Fredrik Berggren,[1] Dmitrii N. Maksimov,[2] and Almas F. Sadreev[1,2]

[1]*IFM–Theory and Modeling, Linköping University, S-581 83 Linköping, Sweden*

[2]*L.V. Kirensky Institute of Physics, 660036, Krasnoyarsk, Russia*

Ruven Höhmann, Ulrich Kuhl, and Hans-Jürgen Stöckmann

AG Quantenchaos, Fachbereich Physik der Philipps-Universität Marburg, Renthof 5, D-35032 Marburg, Germany

This paper reports on a joint theoretical and experimental study of the Pauli quantum-mechanical stress tensor $T_{\alpha\beta}(x,y)$ for open two-dimensional chaotic billiards. In the case of a finite current flow through the system the interior wave function is expressed as $\psi = u + iv$. With the assumption that u and v are Gaussian random fields we derive analytic expressions for the statistical distributions for the quantum stress tensor components $T_{\alpha\beta}$. The Gaussian random field model is tested for a Sinai billiard with two opposite leads by analyzing the scattering wave functions obtained numerically from the corresponding Schrödinger equation. Two-dimensional quantum billiards may be emulated from planar microwave analogs. Hence we report on microwave measurements for an open two-dimensional cavity and how the quantum stress tensor analog is extracted from the recorded electric field. The agreement with the theoretical predictions for the distributions for $T_{\alpha\beta}(x,y)$ is quite satisfactory for small net currents. However, a distinct difference between experiments and theory is observed at higher net flow, which could be explained using a Gaussian random field, where the net current was taken into account by an additional plane wave with a preferential direction and amplitude.

PACS number(s): 05.45.Mt, 03.65.−w, 05.60.Gg

I. INTRODUCTION

Chaotic quantum systems have been found to obey remarkable universal laws related to, e.g., energy levels, eigenfunctions, transition amplitudes or transport properties. These laws are independent of the details of individual systems and depend only on spin and time-reversal symmetries. The universality manifests itself in various statistical distributions, such as the famous Wigner-Dyson distribution for the energy levels in closed systems, the Thomas-Porter distribution for wave-function intensities, wave-function form, conductance fluctuations, etc. (for overviews, see e.g., Refs. [1–4]). Two-dimensional ballistic systems, such as chaotic quantum billiards (quantum dots) have played an important role in the development of quantum chaos. These systems are ideal because they have clear classical counterparts. Nanosized planar electron billiards may be fabricated from high-mobility semiconductor heterostructures such as gated modulation-doped GaAs/AlGaAs and external leads may be attached for the injection and collection of charge carriers [5]. In this way one may proceed continuously from completely closed systems to open ones. Here we will focus on open chaotic systems in which a current flow is induced by external means. Simulations for open chaotic two-dimensional (2D) systems have shown, for example, that there is an abundance of chaotic states that obey generalized wave-function distributions that depend on the degree of openness [6,7]. There are universal distributions and correlation functions for nodal points and vortices [8–11] and the closely related universal distributions [6,12] and correlation functions for the probability current density [13,14].

In this paper we will focus on the Pauli quantum stress tensor (QST) for open planar chaotic billiards and its statistical properties. As we will see QST supplements previous studies of wave-function statistics and flow patterns in an important way as it probes higher-order derivatives (irrespec-

tive of the chosen gauge) and thereby fine details of a wave function. QST was introduced by Pauli [15,16] already in 1933 but in contrast to the corresponding classical entities for electromagnetic fields and fluids [17], for example, it has remained somewhat esoteric since then. On the other hand, studies of stress are in general an important part of material science research and, on a more fundamental atomistic level, stress originates from quantum mechanics. Efficient computational methods based on electronic structure calculations of solids have therefore been developed to analyze both kinetic and configurational contributions to stress [18–20]. The recent advances in nanomechanics also puts more emphasis on the quantum-mechanical nature of stress [21]. Furthermore it features quantum hydrodynamic simulations of transport properties of different quantum-sized semiconductor devices such as resonant tunneling devices (RTD) and high electron mobility transistors (HEMT) [22], and in atomic physics and chemistry [23,24]. All in all, QST is a fundamental concept in quantum mechanics that brings together local forces and the flow of probability density. Hence it is natural to extend the previous studies of generic statistical distributions for open chaotic quantum billiards to also include the case of stress. Our choice of planar ballistic quantum billiards is favorable in this respect as stress is then only of kinetic origin. Moreover, the motion in an open high-mobility billiard may ideally be viewed as interaction free because the nominal two-dimensional mean free path may exceed the dimensions of the billiard itself. In this sense we are dealing, to a good approximation, with single-particle behavior.

There is an ambiguity in the expression for the stress tensor because any divergence-free tensor may be added without affecting the forces [25,26]. For clarifying our definitions and particular choice, we repeat the basic steps, albeit elementary, in Pauli's original derivation of his QST [15,16]. If $\psi(\mathbf{x}, \mathbf{t})$ is a solution to the Schödinger equation

$$i\hbar \frac{\partial \psi}{\partial t} = -\frac{\hbar^2}{2m}\Delta\psi + V\psi, \tag{1}$$

for a particle with mass m moving in the external potential V, the components of the probability current density are

$$j_\alpha = \frac{\hbar}{2mi}\left(\psi^*\frac{\partial \psi}{\partial x_\alpha} - \psi\frac{\partial \psi^*}{\partial x_\alpha}\right). \tag{2}$$

Taking the time derivative of j_α and using the right-hand side of the Schrödinger equation above to substitute $\partial \psi/\partial t$, Pauli arrived at the expression

$$m\frac{\partial j_\alpha}{\partial t} = -\sum_\beta \frac{\partial T_{\alpha\beta}}{\partial x_\beta} - \frac{\partial V}{\partial x_\alpha}|\psi|^2, \tag{3}$$

where $T_{\alpha\beta}$ is his form of the quantum-mechanical stress tensor

$$T_{\alpha\beta} = \frac{\hbar^2}{4m}\left(-\psi^*\frac{\partial^2 \psi}{\partial x_\alpha\,\partial x_\beta} - \psi\frac{\partial^2 \psi^*}{\partial x_\alpha\,\partial x_\beta} + \frac{\partial \psi}{\partial x_\alpha}\frac{\partial \psi^*}{\partial x_\beta} + \frac{\partial \psi^*}{\partial x_\alpha}\frac{\partial \psi}{\partial x_\beta}\right). \tag{4}$$

In the case of planar billiards, V may be set equal to zero, and it is in that form that we will explore Eq. (4). The kinetic Pauli QST is sometimes referred to as the quantum-mechanical momentum flux density, see, e.g., Ref. [20]. From now on we will simply refer to it as QST.

There are obvious measurement problems associated with QST for a quantum billiard, among them the limited spatial resolution presently available (see, e.g., Ref. [27]). In the case of 2D quantum billiards there is, however, a beautiful way out of this dilemma, a way that we will follow here. It turns out that single-particle states ψ in a hard-wall quantum billiard with constant inner potential obey the same stationary Helmholtz equation and same boundary condition as states in a flat microwave resonator [1]. This means that our quantum billiard can be emulated from microwave analogs in which the perpendicular electric field E_z takes the role of the wave function ψ. Since the electric field may be measured this kind of emulation gives us a unique opportunity to inspect the interior of a quantum billiard experimentally [28–33]. Using the one-to-one correspondence between the Poynting vector and the probability current density, probability densities and currents have been studied in a microwave billiard with a ferrite insert as well as in open billiards. Distribution functions based on measurements were obtained for probability densities, currents, and vorticities. In addition, vortex pair correlation functions have been extracted. For all quantities studied [4,13,14] complete agreement was obtained with predictions based on the assumption that wave functions in a chaotic billiard may be represented by a random superposition of monochromatic plane waves [34].

The layout of the paper is the following. In Sec. II we outline the meaning of QST by referring to Madelung's hydrodynamic formulation of quantum mechanics from 1927 [35]. Section III presents the derivation of the distribution functions for the components of the QST in 2D assuming that the wave function may be described in terms of a random Gaussian field and that the net current is zero. Although

our focus is on 2D, the results are extended to three dimensional (3D) as well. Section IV deals with the distribution of the quantum potential that appears naturally in the hydrodynamic formulation of quantum mechanics. In Sec. V we present numerical simulations of transport through an open Sinai billiard with two opposite leads and a comparison with the analytical Gaussian random field model is made. Microwave measurements are reported in Sec. VI and analyzed in terms of the quantum stress tensor. A Berry-type wave function with directional properties is introduced in the same section to analyze the influence of net currents on the statistical distributions for $T_{\alpha\beta}(x,y)$.

II. MEANING OF QST

One of the earliest physical interpretations of the Schrödinger equation is due to Madelung who introduced the hydrodynamic formulation of quantum mechanics already in 1927 [35]. This is a helpful step to get a more intuitive understanding in classical terms of, for example, quantum-mechanical probability densities and the meaning of quantum stress (see, e.g., Refs. [36–38]). Madelung obtained the quantum-mechanical (QM) hydrodynamic formulation by rewriting the wave function ψ in polar form as

$$\psi(\mathbf{x},t) = R(\mathbf{x},t)e^{iS(\mathbf{x},t)/\hbar}. \tag{5}$$

The probability density is then $\rho = R^2$. By introducing the velocity $\mathbf{v} = \nabla S(\mathbf{x},t)/m$ the probability density current or probability flow is simply $\mathbf{j} = \rho\mathbf{v}$. Intuitively this is quite appealing. Inserting the polar form in the Pauli expression for $T_{\alpha\beta}$ in Eq. (4) we then have

$$T_{\alpha,\beta} = \frac{\hbar^2}{4m}\left(-\frac{\partial^2 \rho}{\partial x_\alpha x_\beta} + \frac{1}{\rho}\frac{\partial \rho}{\partial x_\alpha}\frac{\partial \rho}{\partial x_\beta}\right) + \rho m v_\alpha v_\beta. \tag{6}$$

There are two qualitatively different terms in Eq. (6), a quantum-mechanical term $\tilde{T}_{\alpha\beta}$ that contains the factor $\hbar$ and therefore vanishes in the classical limit $\hbar \to 0$, plus the classical contribution $\rho m v_\alpha v_\beta$ which remains in the classical limit. Using the notations above Eq. (3) gives the quantum hydrodynamic analog of the familiar classical Navier-Stokes equation for the flow of momentum density $m\rho\mathbf{v}$,

$$m\frac{\partial \rho v_\alpha}{\partial t} = -\sum_\beta \nabla_\beta T_{\alpha\beta} - \rho\nabla_\alpha V. \tag{7}$$

Alternatively the Schrödinger equation may be rewritten as the two familiar hydrodynamic equations in the Euler frame [36–38],

$$\frac{\partial \rho}{\partial t} + \boldsymbol{\nabla}\cdot[\rho\mathbf{v}] = 0, \tag{8}$$

$$\frac{\partial \mathbf{v}}{\partial t} + [\mathbf{v}\cdot\boldsymbol{\nabla}]\mathbf{v} = \mathbf{f}/m + \mathbf{F}/m, \tag{9}$$

where the external force is due to external potential

$$\mathbf{f} = -\boldsymbol{\nabla}V, \tag{10}$$

and the internal force is due to the quantum potential

$$\mathbf{F} = -\boldsymbol{\nabla} V_{\mathrm{QM}}, \quad V_{\mathrm{QM}} = -\frac{\hbar^2}{2m}\frac{\nabla^2 R}{R}. \tag{11}$$

Then the internal force can be expressed by a stress tensor for the probability fluid as

$$F_\alpha = -\sum_\beta \frac{1}{\rho}\frac{\partial \widetilde{T}_{\alpha\beta}}{\partial x_\beta}. \tag{12}$$

Thus we are dealing with a "probability fluid" in which flow lines and vorticity patterns are closely related to QST.

III. DISTRIBUTION OF QST FOR A QUANTUM BILLIARD

We now return to the full expression for the stress tensor $T_{\alpha\beta}$ in Eq. (4). Consider a flat two-dimensional ballistic cavity (quantum dot) with hard walls. Within the cavity we therefore have $V=0$ and the corresponding Schrödinger equation is $(\Delta+k^2)\psi(x,y)=0$ with $k^2=2mE/\hbar^2$, where k is the wave number at energy E. In this case the wave function may be chosen to be real if the system is closed and, as a consequence, there is no interior probability density flow. The wave function normalizes to one over the area A of the cavity. On the other hand, if the system is open, for example, by attaching external leads, and there is a net transport, the wave function must be chosen complex. Thus,

$$\psi \to u + iv, \tag{13}$$

in which u and v independently obey the stationary Schrödinger equation for the open system. In the following discussion it is convenient to make a substitution to dimensionless variables, $k\mathbf{x}\to\mathbf{x}'$. Hence, we have $(\Delta' +1)u(x',y')=0$ and similarly for $v(x',y')$. The size of the cavity scales accordingly as $A\to A'$.

If the shape of the cavity is chaotic we may assume that u and v are to a good approximation random Gaussian functions (RGFs) [6,39] with $\langle u^2+v^2\rangle=1+\epsilon^2$, $\langle v^2\rangle=\epsilon^2\langle u^2\rangle$, $\langle uv\rangle =0$, and $\langle u\rangle=\langle v\rangle=0$. If u and v were correlated we can apply a phase transformation [6] which makes these functions uncorrelated. Here, we use the definition

$$\langle\cdots\rangle = \frac{1}{A}\int\cdots dA = \frac{1}{A'}\int\cdots dA'. \tag{14}$$

In what follows we thus use dimensionless derivatives in $\mathbf{x}'$ and express the QST components in units of the energy $\hbar^2 k^2/2m$. From Eq. (4), dropping the prime in the expressions from now on, we then have

$$T_{xx} = -u\frac{\partial^2 u}{\partial^2 x} - v\frac{\partial^2 v}{\partial^2 x} + \left(\frac{\partial u}{\partial x}\right)^2 + \left(\frac{\partial v}{\partial x}\right)^2 \tag{15}$$

and

$$T_{xy} = -u\frac{\partial^2 u}{\partial x\,\partial y} - v\frac{\partial^2 v}{\partial x\,\partial y} + \frac{\partial u}{\partial x}\frac{\partial u}{\partial y} + \frac{\partial v}{\partial x}\frac{\partial v}{\partial y}. \tag{16}$$

Two-dimensional case. Let us first consider the distributions of the stress tensor for a two-dimensional complex RGF ψ. In the following derivation we assume that the net

current from one lead to the other is so small that in practice we are dealing with isotropic RGFs. We therefore have

$$\langle uu_{xx}\rangle = -\frac{1}{2}, \quad \langle u_x^2\rangle = \frac{1}{2}, \quad \langle uu_x\rangle = 0,$$

$$\langle u_x u_{xx}\rangle = 0, \quad \langle u_{xx}^2\rangle = \frac{3}{8} \tag{17}$$

for the two-dimensional case. The corresponding expressions for v follow simply by replacing u, u_x, u_{xx}, etc., by $v/\epsilon, v_x/\epsilon, v_{xx}/\epsilon$, and so on.

For the component T_{xx} in Eq. (15) we need the following joint distribution of two RGFs [40]:

$$f(\vec{X}) = \frac{1}{2\pi\sqrt{\det(K)}}\exp\left(-\frac{1}{2}\vec{X}^\dagger K^{-1}\vec{X}\right), \tag{18}$$

where $\vec{X}^\dagger = (u, v, u_x, v_x, u_{xx}, v_{xx})$, and the matrix $K=\langle\vec{X}\vec{X}^\dagger\rangle$. For an isotropic RGF there are only correlations $\langle uu_{xx}\rangle$, $\langle vv_{xx}\rangle$. Therefore, the only nontrivial block of the total matrix K is the matrix

$$K_u = \begin{pmatrix} 1 & -1/2 \\ -1/2 & 3/8 \end{pmatrix}, \quad K_u^{-1} = \begin{pmatrix} 3 & 4 \\ 4 & 8 \end{pmatrix} \tag{19}$$

for the RGFs u, u_{xx} and the matrix $K_v = \epsilon K_u$ for the two RGFs for v and v_{xx}. Correspondingly we obtain from Eq. (18),

$$f(u,u_{xx}) = \frac{\sqrt{8}}{2\pi}\exp\left(-\frac{3u^2 + 8uu_{xx} + 8u_{xx}^2}{2}\right) \tag{20}$$

and

$$f(v,v_{xx}) = \frac{\sqrt{8}}{2\pi\epsilon^2}\exp\left(-\frac{3v^2 + 8vv_{xx} + 8v_{xx}^2}{2\epsilon^2}\right). \tag{21}$$

The characteristic function of the stress tensor component T_{xx} is

$$\theta(a) = \langle e^{iaT_{xx}}\rangle \tag{22}$$

and takes the following explicit form:

$$\theta(a) = 8\{(1-ia)(1-i\epsilon a)[a-i(\sqrt{24}+4)][\epsilon a - i(\sqrt{24}+4)]$$
$$\times[a+i(\sqrt{24}-4)][\epsilon a - i(\sqrt{24}-4)]\}^{-1/2}. \tag{23}$$

As a result we obtain for the distribution function

$$P(T_{xx}) = \frac{1}{2\pi}\int_{-\infty}^{\infty}\theta(a)e^{-iaT_{xx}}da. \tag{24}$$

For $\epsilon\neq 1$ this integral may be calculated numerically. However, for $\epsilon=1$ it might be evaluated analytically. In particular, for $T_{xx}>0$ we obtain

$$P(T_{xx}) = \frac{2}{\sqrt{6}}\frac{e^{-(\sqrt{24}-4)T_{xx}}}{(5-\sqrt{24})} - 8e^{-T_{xx}}, \tag{25}$$
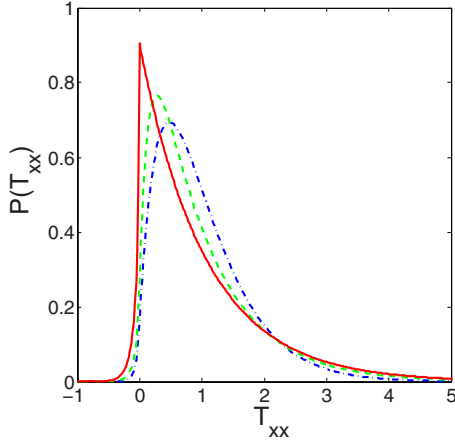
and for $T_{xx}<0$,

FIG. 1. (Color online) The distribution $P(T_{xx})$ for $\epsilon=1$ (dashed-dotted line), $\epsilon=0.5$ (dashed line), and $\epsilon=0$ (solid line). The stress tensor component T_{xx} is measured in terms of the mean value $\langle T_{xx} \rangle$.

$$P(T_{xx}) = \frac{2}{\sqrt{6}} \frac{e^{(\sqrt{24}+4)T_{xx}}}{(5+\sqrt{24})}. \tag{26}$$

The distribution (26) is shown in Fig. 1 together with results for different ϵ values obtained by numerical evaluation of the integral (24). Note that the distributions are here given in terms of $\langle T_{xx} \rangle = 1 + \epsilon^2$.

To repeat the calculations for the component T_{xy} we need the following correlators:

$$\langle uu_{xy} \rangle = 0, \quad \langle u_x u_{xy} \rangle = 0, \quad \langle u_y u_{xy} \rangle = 0, \quad \langle u_{xy}^2 \rangle = \frac{1}{8} \tag{27}$$

for the 2D case. The correlation matrix turns out to be diagonal. Then the characteristic function

$$\theta(a) = 2\{[2+(a/2)^2][2+(\epsilon a/2)^2][1+(a/2)^2] \\ \times [1+(\epsilon a/2)^2]\}^{-1/2} \tag{28}$$

defines the distribution $P(T_{xy})$. For $\epsilon=1$ the integral (24) may, as above, be performed analytically to give

$$P(T_{xy}) = 2e^{-2|T_{xy}|} - \sqrt{2}e^{-2\sqrt{2}|T_{xy}|}. \tag{29}$$

The distributions $P(T_{xy})$ in Eq. (29) are shown in Fig. 2 for the two cases $\epsilon=0$ and $\epsilon=1$. Only two cases are shown because of the small differences in $P(T_{xy})$ for different ϵ values. The distributions are in this case given in terms of $\sqrt{\langle T_{xy}^2 \rangle}$, where $\langle T_{xy}^2 \rangle = \frac{3}{8}(1+\epsilon^4)$.

Three-dimensional case. In this case the expressions in Eq. (17) are to be replaced by

$$\langle uu_{xx} \rangle = -\frac{1}{3}, \quad \langle u_x^2 \rangle = \frac{1}{3},$$

$$\langle uu_x \rangle = 0, \quad \langle u_x u_{xx} \rangle = 0, \quad \langle u_{xx}^2 \rangle = \frac{1}{5}, \tag{30}$$
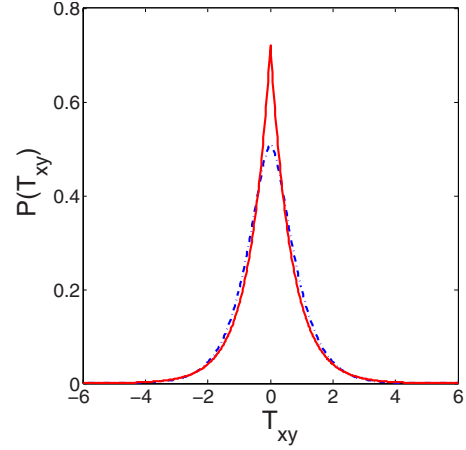
and Eq. (27) by

FIG. 2. (Color online) The distribution $P(T_{xy})$ for $\epsilon=1$ (dashed-dotted line) and $\epsilon=0$ (solid line). The stress tensor component T_{xy} is measured in terms of mean value $\sqrt{\langle T_{xy}^2 \rangle}$.

$$\langle uu_{xy} \rangle = 0, \quad \langle u_x u_{xy} \rangle = 0, \quad \langle u_y u_{xy} \rangle = 0, \quad \langle u_{xy}^2 \rangle = \frac{1}{15}. \tag{31}$$

Accordingly the correlation matrix (19) is

$$K_u = \begin{pmatrix} 1 & -1/3 \\ -1/3 & 1/5 \end{pmatrix}, \quad K_u^{-1} = \frac{1}{4}\begin{pmatrix} 9 & 15 \\ 15 & 45 \end{pmatrix}. \tag{32}$$

The joint probability function of two RGFs u and u_{xx} then takes the following form:

$$f(u, u_{xx}) = \frac{\sqrt{45}}{2\pi} \exp\left(-\frac{9u^2 + 30uu_{xx} + 45u_{xx}^2}{8}\right). \tag{33}$$

The characteristic function defining the distribution $P(T_{xx})$ is

$$\theta(a) = \frac{45}{(3/2-ia)(ia+15/4+9\sqrt{5}/4)} \frac{1}{(ia+15/4-9\sqrt{5}/4)} \tag{34}$$

and, correspondingly,

$$P(T_{xx}) = \frac{5}{(7\sqrt{5}-15)} e^{-(9\sqrt{5}-15/4)T_{xx}} - \frac{15}{2} e^{-(3/2)T_{xx}} \tag{35}$$

for $T_{xx} > 0$, and

$$P(T_{xx}) = \frac{5}{(7\sqrt{5}+15)} e^{(9\sqrt{5}+15/4)T_{xx}} \tag{36}$$

for $T_{xx} < 0$. Identical expressions hold for the two other diagonal components.

In a similar way we obtain the distribution function for the off-diagonal components $\alpha \neq \beta$. For the specific case $\epsilon=1$ we have, according to Eq. (31),

$$\theta(a) = \frac{2}{[3+(a/2)^2][1+(a/2)^2]} \tag{37}$$

and

$$P(T_{xy}) = \frac{15}{4}e^{-3|T_{xy}|} - \frac{3\sqrt{15}}{4}e^{-\sqrt{15}|T_{xy}|}. \tag{38}$$

The expression for the other off-diagonal components are, of course, identical.

IV. DISTRIBUTION OF QUANTUM POTENTIAL

The quantum or internal force in Eq. (11) in the hydrodynamic formulation is defined by the quantum potential V_{QM}. In terms of the RGFs u, v it may be written as

$$V_{QM} = -V_x - V_y,$$

$$V_x = \frac{uu_{xx} + vv_{xx} + u_x^2 + v_x^2}{u^2 + v^2} - \left(\frac{uu_x + vv_x}{u^2 + v^2}\right)^2,$$

$$V_y = \frac{uu_{yy} + vv_{yy} + u_y^2 + v_y^2}{u^2 + v^2} - \left(\frac{uu_y + vv_y}{u^2 + v^2}\right)^2. \tag{39}$$

The second derivatives might be eliminated using the Schrödinger equations for u and v, i.e., $u_{xx} + u_{yy} = -u$, $v_{xx} + v_{yy} = -v$. As a result we have

$$V_{QM} = 1 - \frac{(uv_x - vu_x)^2 + (uv_y - vu_y)^2}{\rho^2}, \tag{40}$$

which implies

$$-\infty \leq V_{QM} \leq 1. \tag{41}$$

The distribution of the quantum potential is given by

$$P(V_{QM}) = \frac{1}{2\pi} \int \exp(-iaV_{QM}) \theta(a) da, \tag{42}$$

where

$$\theta(a) = \langle \exp(iaV_{QM}) \rangle = \int d^6 \vec{X} f(\vec{X}) \exp(iaV_{QM}), \tag{43}$$

$f(\vec{X})$ is given by the same formula as Eq. (18), however, with vector $\vec{X}^+ = (u, v, u_x, v_x, u_y, v_y)$ with the same correlators as Eq. (19).

For Eq. (43) we may now write with $\epsilon = 1$, which is the only case accessible in closed analytic form,

$$\theta(a) = \frac{1}{2\pi} \int du dv \Gamma_x \Gamma_y \exp\left(-\frac{1}{2}(u^2 + v^2) + ia\right), \tag{44}$$

with

$$\Gamma_x = \frac{1}{\pi} \int du_x dv_x \exp\left(-u_x^2 - v_x^2 + \frac{ia(uu_x - vv_x)^2}{\rho^2}\right). \tag{45}$$

The same expression holds for Γ_y. The integration in Eq. (45) gives

$$\Gamma_x \Gamma_y = \frac{-i\rho}{a - i\rho}. \tag{46}$$

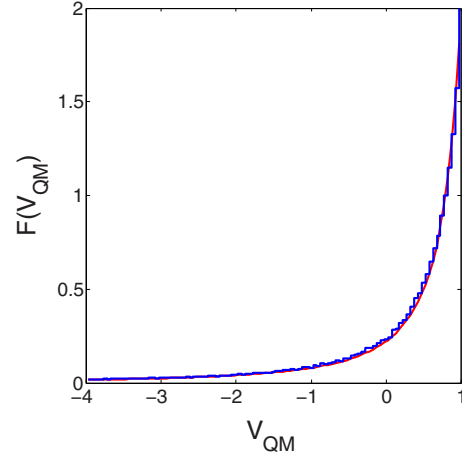Substituting Eq. (46) into Eq. (44) we obtain

FIG. 3. (Color online) The distribution of the quantum potential (48) for $\epsilon = 1$ compared to numerical histogram based on the Berry function in Eq. (49).

$$\theta(a) = -i \int_0^\infty \frac{dr r^3}{a - ir^2} \exp(ia - r^2/2), \tag{47}$$

where $r = \sqrt{\rho}$. Finally, substituting that into Eq. (42) we obtain the distribution function for the quantum potential

$$P(V_{QM}) = \frac{1}{2(3/2 - V_{QM})^2}. \tag{48}$$

The distribution (48) is normalized as $\int_{-\infty}^1 P(V)dV = 1$. The distribution of $P(V_{QM})$ is shown in Fig. 3 and compared to a numerical computation of the same statistics based on the Berry conjecture for chaotic wave functions [34]

$$\psi(r) = \frac{1}{\sqrt{A}} \sum_n a_n e^{i\mathbf{k}_n \cdot \mathbf{r}}. \tag{49}$$

Here A is the area of the random monochromatic plane wave field with $|\mathbf{k}_n|^2 = 1$ and the amplitudes for the random plane waves obey the relation $\langle a_n^2 \rangle = \frac{1}{N}$. The Berry function in Eq. (49) corresponds to $\epsilon = 1$.

V. NUMERICAL SIMULATIONS OF SCATTERING STATES IN AN OPEN CHAOTIC ELECTRON BILLIARD

A billiard becomes an open one when it is connected to external reservoirs, for example, via attached leads. A stationary current through the system may be induced by applying suitable voltages to the reservoirs (or by a microwave power source as in Sec. VI). Here we consider hard-walled Sinai-type billiards with two opposite normal leads. A first step toward a numerical simulations of the quantum stress tensor is to find the corresponding scattering states by solving the Schrödinger equation $-\nabla^2 \psi = k^2 \psi$ for the entire system. The numerical procedure for this is well known. Thus, we use the finite difference method for the interior of the billiard in combination with the Ando boundary condition [10,41] for incoming, reflected, and transmitted solutions in the straight leads. Once a scattering wave function has been computed in this way the fraction residing in the cavity itself
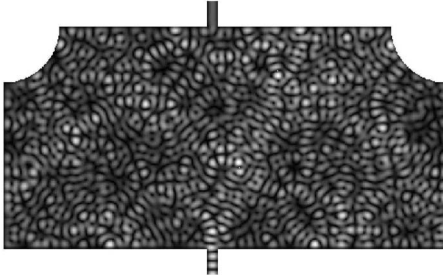
FIG. 4. View of the scattering wave function in the open Sinai billiard for the case A shown in Fig. 5 for $k^2=30.878$ in dimensionless units (see text) and for small aspect ratio $d/L=2/67$ (ratio between the widths of the leads and the billiard). The system is asymmetric because the two opposite leads are slightly off the middle symmetry line of the nominal billiard. Only the lowest channel is open in the leads.

is extracted for the statistical analysis. To ensure statistical independence of the real and imaginary parts u and v a global phase is removed as discussed in Ref. [6]. By this step we also find the value of ϵ. The interior wave function is then normalized as defined in Sec. III.

For the numerical work it is convenient to make the substitution $x \rightarrow x/d$ and $y \rightarrow y/d$, where d is the width of the leads. Here we use dimensionless energy $k^2=E/E_0$, $E_0 = \hbar^2/(2md^2)$. (In the case of a semiconductor billiard referred to in the introduction, the mass m should be the effective conduction band mass m^*.) Below we consider the specific case of small wavelengths λ as shown in Fig. 4. We will also comment on the case when λ is large compared to the dimensions of the cavity.

To ensure that the scattering wave function complies with a complex RGF we consider a small aspect ratio d/L as in Fig. 4 (see also Ref. [10]). The actual numerical size of the Sinai billiard in Fig. 4 is chosen as follows: Height 346 (along transport), width (L) 670, radius 87, and 20 for the number of grid points across the wave guides (d). Within this configuration we now only excite scattering wave functions with characteristic wavelengths $\lambda \ll L$. As expected from Fig. 4 the wave function statistics show that both real and imaginary parts, u and v, obey Gaussian statistics to a high degree of accuracy. Results for transmission T and ϵ are shown in Fig. 5.

The corresponding distributions for the QST components are given in Figs. 6 and 7 supplemented by the distributions for j_x with the x axis directed along transport. There is indeed an overall good agreement between theory and simulations. However, in the statistics for j_x in Fig. 6 one notices a tiny difference at small values of j_x. The reason is that there is a net current at this value of ϵ, which is not incorporated in our choice of analytic isotropic RGFs. The deviation is, however, much too small to have an impact on the statistical analysis presented here because the net current is such a tiny fraction of the entire current pattern within the cavity. The case B with $\epsilon=0$ implies that the scattering wave function in the cavity is real (standing wave with transmission $T=0$ as seen from Fig. 5). Therefore, there is no current within the cavity.

The agreement with the analytic results for RGFs and the present numerical modeling for billiards of finite size is ob-
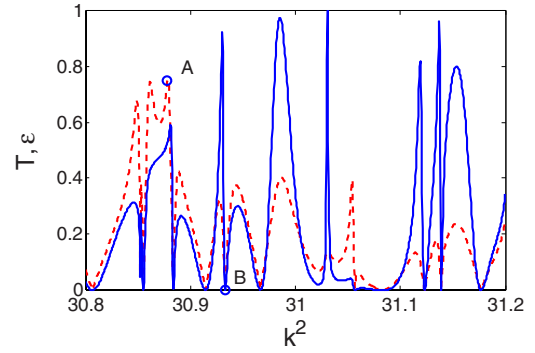

FIG. 5. (Color online) The transmission probability T (solid line) and ϵ (dashed line) as function of the dimensionless energy k^2 for the Sinai billiard in Fig. 4. Two open circles show case A with maximal $\epsilon=0.75$ and case B with the minimal $\epsilon=0$. At most only one channel is open in the leads.

viously good in the range of energies explored here. In order to smooth fluctuations in the distributions of the stress tensor we have averaged over the energy window shown in Fig. 5 (without scaling ϵ to 1 in contrast to Fig. 11 of Sec. VI). In this way one finds a perfect agreement between theory and numerical simulations as shown in Fig. 8. For future reference we note that the presence of net currents through the billiard appears to have little or no influence on the distributions for the present two-lead configuration and choice of energy range. We also note that the present results are not sensitive to the position of the leads. For example, we have also performed simulations for Sinai billiards with one dent only and with the leads attached at corners.

We now turn to the complementary case of long wavelengths (low energies). The low-energy regime is achieved for large aspect ratio d/L which selects wave functions with
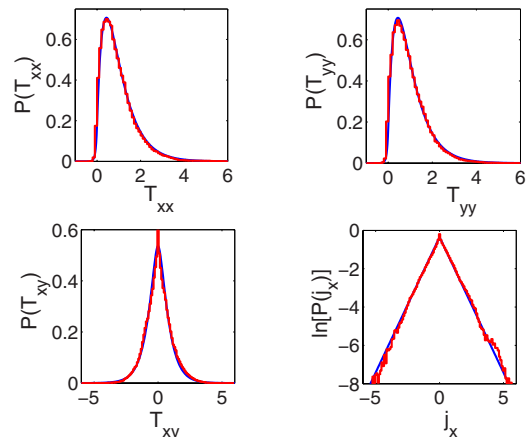

FIG. 6. (Color online) Analytic and numerically simulated distributions of the components of the QST and probability density current j_x along the transport axis for the case A shown in Fig. 5 ($\epsilon=0.75$). As in Figs. 1 and 2 the diagonal components are measured in terms of their mean values while T_{xy} and j_x are given in terms of $\sqrt{\langle T_{xy}^2 \rangle}$ and $\sqrt{\langle j_x^2 \rangle}$, respectively. Solid lines refer to analytic results for RGFs (Sec. III and Ref. [6]) and histograms to the present numerical modeling. Because of the close agreement between the two cases, differences are barely resolved.
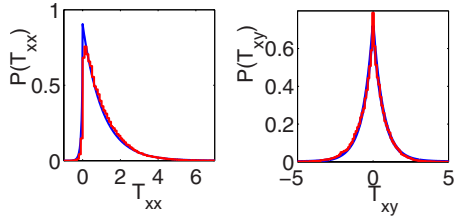
FIG. 7. (Color online) Analytic and numerically simulated distributions of the components of the QST for the case B in Fig. 5 ($\epsilon=0$). The simulated distribution for T_{yy} is nearly identical to $P(T_{xx})$ and therefore not shown here. Because ϵ vanishes there is not any current within the cavity. (The choice of lines in the graphs and units are the same as in Fig. 6. Because of the close agreement between theory and simulations, differences are hardly noticeable.)

λ a few times less than L. Moreover a low-energy incoming wave often excites bouncing modes. Numeric's for the case $k^2=12$ and large aspect ratio $d/L=1/7$ show that the scattering wave function may be rather different from a complex RGF. Hence, the corresponding distributions for individual states deviate appreciably from the theoretical RGF predictions in Sec. III. However, by averaging over a wide energy window, as above, one closes in on theory. In this way one introduces an ensemble that, for practical purposes, mimics the random Gaussian case. This aspect may be useful in experimental circumstances in which the short wavelength limit might be hard to achieve.

VI. EXPERIMENTAL STUDIES

In quasi-2D resonators there is, as outlined in the introduction, a one-to-one correspondence between the transverse modes (TM) of the electromagnetic field and the wave functions of the corresponding quantum billiard [1]. The z component of the electromagnetic field E_z corresponds to the quantum-mechanical wave function ψ, and the wave number $k^2=\omega^2/c^2$ to the quantum-mechanical eigenenergy, where ω is the angular frequency of the TM mode and c the speed of light. In the present study a rectangular cavity (16 cm $\times$ 21 cm) with rounded corners has been used, with two attached leads with a width of 3 cm. Antennas placed in the leads acted as source and drain for the microwaves (see Fig.
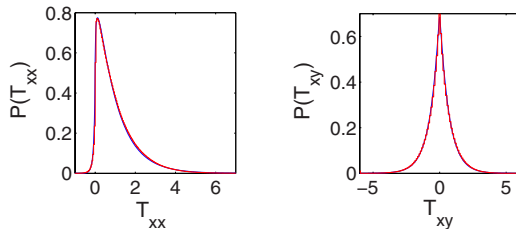

FIG. 8. (Color online) Analytic and numerically simulated distributions of the components of stress tensor T_{xx} and T_{xy} averaged over the energy window given in Fig. 5. The theoretical curves are obtained also by averaging over computed ϵ values shown in Fig. 5. (The choice of lines and units are the same as in Fig. 6. The agreement between theory and simulations is excellent, hence any small differences are not resolved on the scale shown here.)
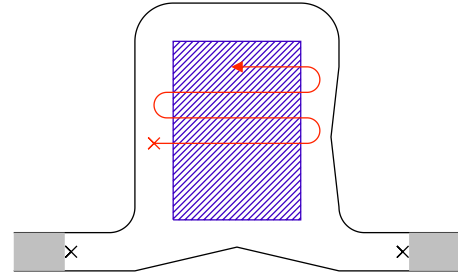

FIG. 9. (Color online) Sketch of the microwave billiard. The basic size of the billiard is 16 cm $\times$ 21 cm. The attached leads have a width of 3 cm. The central shaded field (10 cm $\times$ 14 cm) indicates the region where the data have been collected. The measurement grid size was 2.5 mm. The gray regions at the end of the two leads indicate absorbers to mimic infinitely long channels. The crosses indicate the antennas in the system and the winding path illustrates how the third probing antenna is moved across the billiard during measurements.

9). Two wedge-shaped obstacles had been attached to two sides of the billiard to avoid any bouncing ball structures in the measurement. The same system has been used already for the study of a number of transport studies [13,14] and for the statistics of nodal domains and vortex distributions [42]. A more detailed description of the experimental setup can be found in Ref. [43]. The field distribution inside the cavity has been obtained via a probe antenna moved on a grid with a step size of 2.5 mm. To avoid boundary effects, only data from the shaded region (see Fig. 9) has been considered in the analysis.

The transmission from the source to the probe antenna has been measured on the frequency range from 5.5 to 10 GHz with a step size of 20 MHz, corresponding to wavelengths from 3 to 5 cm. The transmission is proportional to the electric field strength, i.e., to the wave function, at the position of the probe antenna. This assumes that the leak current into the probe antenna may be neglected.

To check this we compared the experimentally obtained distribution of wave function intensities $\rho=|\psi|^2$ with the modified Porter-Thomas distribution (see, e.g., Ref. [6]),

$$p(|\psi|^2) = \mu \exp(-\mu^2|\psi|^2)I_0(\mu\sqrt{\mu^2-1}|\psi|^2), \quad (50)$$

where

$$\mu = \frac{1}{2}\left(\epsilon+\frac{1}{\epsilon}\right) \quad \text{and} \quad \epsilon^2 = \langle v^2\rangle/\langle u^2\rangle. \quad (51)$$

Here ϵ has not been fitted, but was taken directly from the experimentally obtained values for $\langle u^2\rangle$ and $\langle v^2\rangle$, where we have ensured that $\langle uv\rangle=0$ by applying a proper phase rotation as in Ref. [6] and commented on in Sec. V. Whenever χ^2, the weighted squared difference of the experimental data and the modified Porter-Thomas distribution, was below $\chi_{\text{cutoff}}=1.1$, the pattern has been selected for the final analysis of the statistics for the QST components.

Since the wave functions are experimentally known, including their phases, the quantum-mechanical probability density $\mathbf{j}=\text{Im}\,\psi^*\nabla\psi$, and the components of the QST can be obtained from the measurement. As mentioned, distributions
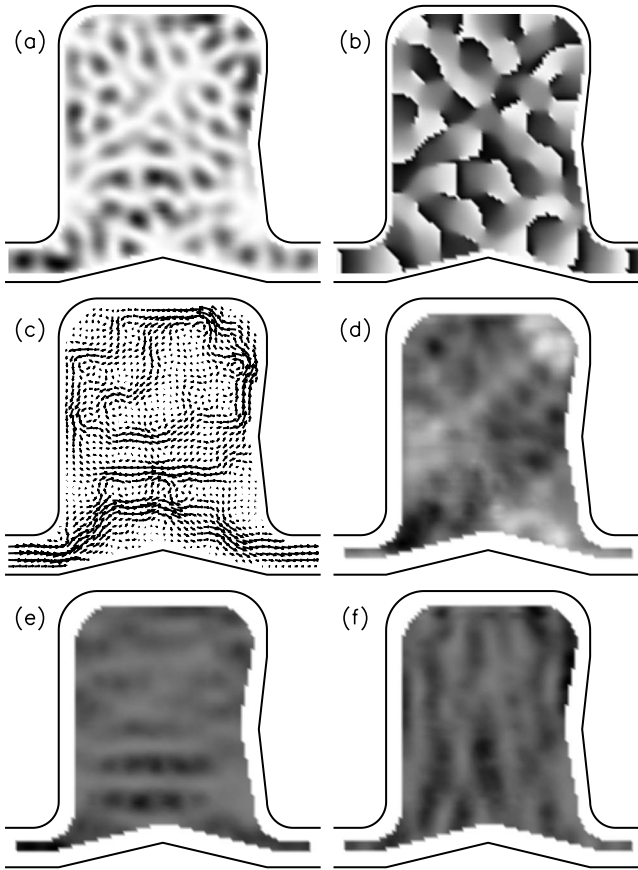
FIG. 10. The figure shows different quantities obtained from the measurement at the frequency $\nu = 8.5$ GHz. In (a) the intensity of the wave function is shown and in (b) its phase. The plot (c) shows the Poynting vector of the system being equivalent to the probability current density in quantum mechanics. In (d)–(f) different components of the QST are shown, namely *xy* (d), *xx* (e), and *yy* component (f). Dark areas indicate higher values.

of current densities and related quantities have already been discussed previously in a number of papers (see, e.g., Refs. [13,14]), but the QST has not been studied experimentally before. As an example, Fig. 10 shows intensity (a) and the phase (b) of the measured field at one frequency, as well as the probability current (c), and different components of the stress tensor (d)–(f).

The analysis of the data has been performed in dimensionless coordinates $\mathbf{x} = k\mathbf{r}$. Since u and v are two independent wave fields we may rescale the imaginary part to obtain ϵ values of one, thus mapping the experimental result to the situation of a completely open billiard. This step made it easy to superimpose the results from many field patterns of different frequencies which originally had different ϵ values. For the analysis all wave functions passing the χ^2 test mentioned above have been used. Altogether 83 of 225 possible patterns have been taken in the analysis.

Figure 11 shows the distribution of the QST components obtained in this way. In addition the theoretical curves are shown as solid lines. From the figure we see that there is a good overall agreement between experiment and theory, but also that nonstatistical deviations are unmistakable.
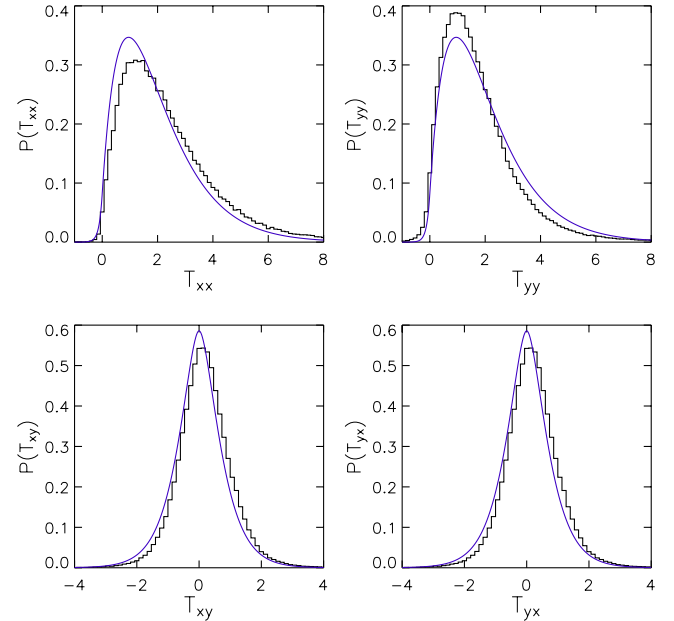

FIG. 11. (Color online) Results for the experimental statistical distributions for the components of the QST stress tensor obtained by a superposition of all experimental data scaled to $\epsilon = 1$ as explained in the text. The solid lines correspond to the theoretical predictions in Sec. III for $\epsilon = 1$.

Deviations between experiment and theory had already been found by us in the past in an open microwave billiard, similar to the one used in the present experiment, in the distribution of current components [13,14]. For the vertical *y* component a complete agreement between experiment and theory was found, but for the horizontal *x* component the experimental distribution showed, in contrast to theory, a pronounced skewness. The origin of this discrepancy was a net current from the left-hand side to the right-hand side due to source and drain in the attached waveguides. In a billiard with broken time-reversal symmetry without open channels, a complete agreement between experiment and theory had been found, corroborating the net current hypothesis.

For a quantitative discussion of the net current we introduced the normalized net current for each pattern

$$\mathbf{j}_{\text{net}} = \frac{\langle \mathbf{j} \rangle}{\langle |\mathbf{j}| \rangle}, \qquad (52)$$

where the average is over all positions in the shaded region in Fig. 9. In Fig. 12 the *y* component of $\mathbf{j}_{\text{net}}$ is plotted versus its *x* component for each wave function. One notices an average net current pointing from the left-hand to the right-hand side, with an angle of about 20° in an upward direction. For the analysis we discriminated between three regimes for the strength of the net current. Additionally we performed a coordinate transformation such that for each pattern the vector of the net current is aligned along the positive *x* axis. This rotation has been done for all experimental and numerical results in this section.

In Fig. 13 the results for the three different regimes of net current strengths are shown. For the distributions of the *xx*
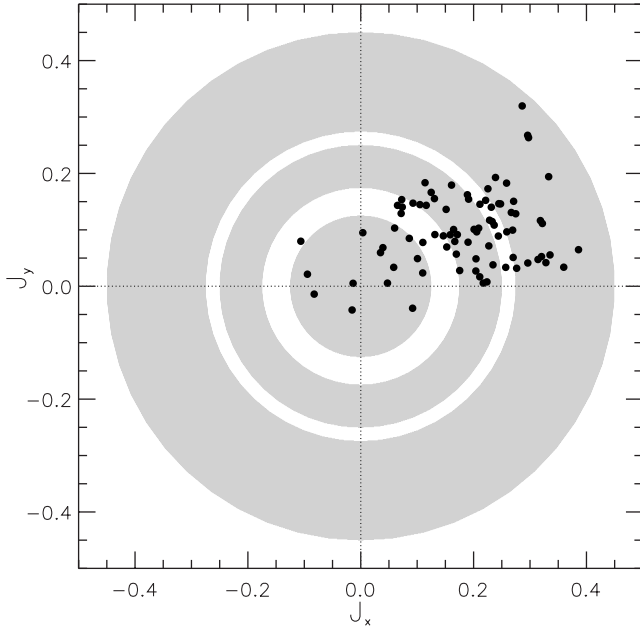
FIG. 12. Plot of the net current as it is defined in Eq. (52). The shaded regions are indicating three different regimes of net current strength which had been used in the later analysis.

and the *yy* component of the QST, a clear dependence on the net current strength is found, where the deviations from theory increase with an increasing net current. T_{xy} is only slightly affected by the net current, if at all. In the limit of a tiny net current, all experimental distributions approach the theoretical ones.
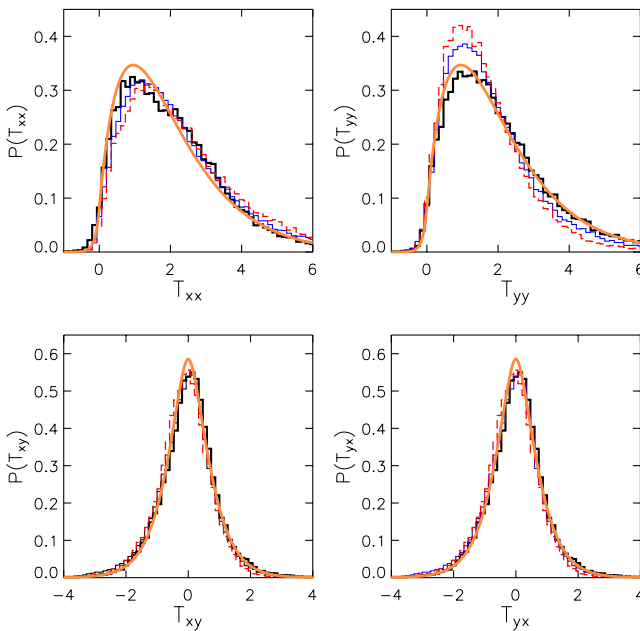
FIG. 13. (Color online) Histograms of the QST distributions obtained from experimental data. The thick lines correspond to the smallest net currents (see Fig. 12), the thin lines to intermediate ones, and the dashed lines to ones with the largest net current. As in Fig. 11 the solid lines correspond to the theoretical predictions in Sec. III for $\epsilon=1$.
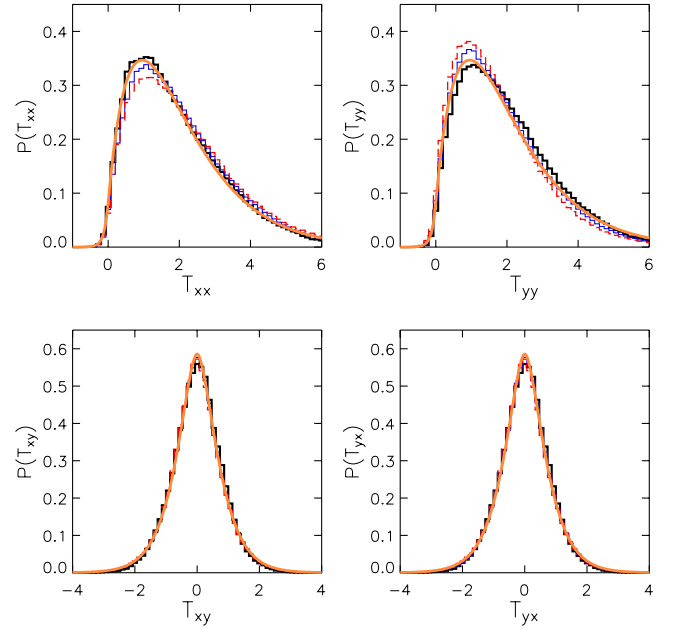

FIG. 14. (Color online) Histograms of the QST components obtained from the simulations according to the wave function in Eq. (53). As in Fig. 13, the thick lines correspond to low, thin to intermediate, and dashed lines to large net currents.

To further test the influence of the net current on the distributions of the stress tensor, we performed a numerical simulation with random plane waves. Each random wave field was calculated on an area of 500 mm $\times$ 500 mm, with a grid size of 2.5 mm. The random wave field consisted of 500 plane waves with random directions and amplitudes. The frequency used for the numerics was $\nu=5$ GHz. To introduce the net current we first performed a random superposition of plane waves according to Eq. (49), and then added a normalized plane wave with the wave vector K' pointing in the same direction as the net current observed in the experiment,

$$\psi(r) = \frac{1}{\sqrt{A}} \left(a' e^{i\mathbf{K}'\cdot\mathbf{r}} + \sum_{n=1}^{N} a_n e^{i\mathbf{k}_n\cdot\mathbf{r}} \right). \tag{53}$$

The strength of the resulting net current was adjusted by a prefactor a'. The best agreement between the experiment and the numeric's was found for $a'=0.45$. To obtain sufficient statistics we averaged over 200 different wave functions. Thus a pattern similar to the one shown in Fig. 12 was obtained with a cloud of dots extending over all three regimes of net current considered with its center in the central regime.

Figure 14 shows the distributions for the QST components for numerical data derived from Eq. (53). The same three regimes as for the experimental study have been used. The results from this type of simulation are in good qualitative agreement with the experimental results. In particular the deviations from the theory in Sec. III increase monotonously with the net current, just as in the experiment.

An obvious question is why these net current effects are unimportant in the simulations for the Sinai billiard pre-

sented in Sec. V. One may argue that the number of independent plane waves entering at a given frequency is given by the circumference of the billiard divided by $\lambda/2$, where λ is the wavelength. Also the width of each wave guide is of the order of $\lambda/2$, i.e., the relative net current is approximately given by the total widths of all openings divided by the circumference of the billiard. Following this argumentation the net current in the experiments amounted to about 10% of the total current, whereas in the simulations for the Sinai billiard it was smaller by a factor of 10; i.e., too small to be of any importance in the simulations.

We have shown that in the limit of small net currents, the distributions of QST components obtained from the experiment are well described by means of the random plane wave model and the analytic distributions in Sec. III. On the other hand, net currents are unavoidable in open systems. As indicated by the simulations for a Sinai billiard in Sec. V, the magnitudes and effect on the different stress tensor distributions may be sensitive to geometry and energy. Hence it remains an open task for theory to incorporate net currents in order to allow for a more realistic comparison with present experimental results.

[1] H.-J. Stöckmann, *Quantum Chaos—An Introduction* (University Press, Cambridge, 1999).

[2] T. Guhr, A. Müller-Groeling, and H. A. Weidenmüller, Phys. Rep. **299**, 189 (1998).

[3] *Quantum Chaos, Y2K—Nobel Symposium 116*, edited by K.-F. Berggren and S. Åberg (Physica Scripta, Stockholm, 2001).

[4] Trends in Quantum Chaotic Scattering, special issue of J. Phys. A **38**, No. 49 (2005), edited by Y. V. Fyodorov, T. Kottos, and H.-J. Stöckmann.

[5] J. H. Davies, *The Physics of Low-dimensional Semiconductors: An Introduction* (Cambridge University Press, Cambridge, 1998).

[6] A. I. Saichev, H. Ishio, A. F. Sadreev, and K.-F. Berggren, J. Phys. A **35**, L87 (2002).

[7] Y.-H. Kim, U. Kuhl, H.-J. Stöckmann, and P. W. Brouwer, Phys. Rev. Lett. **94**, 036804 (2005).

[8] M. V. Berry and M. R. Dennis, Proc. R. Soc. London, Ser. A **456**, 2059 (2000).

[9] A. I. Saichev, K.-F. Berggren, and A. F. Sadreev, Phys. Rev. E **64**, 036222 (2001).

[10] K.-F. Berggren, A. F. Sadreev, and A. A. Starikov, Phys. Rev. E **66**, 016218 (2002).

[11] M. R. Dennis, Eur. Phys. J. Spec. Top. **145**, 191 (2007).

[12] A. F. Sadreev and K.-F. Berggren, Phys. Rev. E **70**, 026201 (2004).

[13] M. Barth and H.-J. Stöckmann, Phys. Rev. E **65**, 066208 (2002).

[14] Y.-H. Kim, M. Barth, U. Kuhl, and H.-J. Stöckmann, Prog. Theor. Phys. Suppl. **150**, 105 (2003).

[15] W. Pauli, *Quantentheorie, Handbuch der Physik XXIV* (Springer, Berlin, 1933).

[16] W. Pauli, *Handbuch der Physik XXIV* (Springer, Berlin, 1980).

[17] C. W. Misner, K. S. Thorne, and J. A. Wheeler, *Gravitation* (W. H. Freeman, New York, 1973).

[18] O. H. Nielsen and R. M. Martin, Phys. Rev. B **32**, 3780 (1985).

[19] N. O. Folland, Phys. Rev. B **34**, 8296 (1986).

[20] M. J. Godfrey, Phys. Rev. B **37**, 10176 (1988).

[21] V. B. Shenoy, in *The Handbook of Nanotechnology: Nanometer Structures, Theory, Modeling and Simulations*, edited by A. Lakhtakia (SPIE, New York, 2004), pp. 256–316.

[22] J. Höntschel, R. Stenzel, and W. Klix, IEEE Trans. Electron Devices **51**, 684 (2004).

[23] M. J. Godfrey, J. Phys. B **23**, 2427 (1990).

[24] J. Tao, G. Vignale, and I. V. Tokatly, Phys. Rev. Lett. **100**, 206405 (2008).

[25] C. L. Rogers and A. M. Rappe, Phys. Rev. B **65**, 224117 (2002).

[26] R. Maranganti, P. Sharma, and L. Wheeler, J. Aerosp. Eng. **20**, 22 (2007).

[27] R. Crook, C. G. Smith, A. C. Graham, I. Farrer, H. E. Beere, and D. A. Ritchie, Phys. Rev. Lett. **91**, 246803 (2003).

[28] S. Sridhar, Phys. Rev. Lett. **67**, 785 (1991).

[29] J. Stein and H.-J. Stöckmann, Phys. Rev. Lett. **68**, 2867 (1992).

[30] A. Gokirmak, D.-H. Wu, J. S. A. Bridgewater, and S. M. Anlage, Rev. Sci. Instrum. **69**, 3410 (1998).

[31] H.-M. Lauber, P. Weidenhammer, and D. Dubbers, Phys. Rev. Lett. **72**, 1004 (1994).

[32] C. Dembowski, H.-D. Gräf, R. Hofferbert, H. Rehfeld, A. Richter, and T. Weiland, Phys. Rev. E **60**, 3942 (1999).

[33] D. Laurent, O. Legrand, P. Sebbah, C. Vanneste, and F. Mortessagne, Phys. Rev. Lett. **99**, 253902 (2007).

[34] M. V. Berry, J. Phys. A **10**, 2083 (1977).

[35] E. Madelung, Z. Phys. **40**, 322 (1927).

[36] I. Bialynicki-Birula, M. Cieplak, and J. Kaminski, *The Theory of Quanta* (Oxford University Press, Oxford, 1992).

[37] P. R. Holland, *The Quantum Theory of Motion: An Account of the de Broglie-Bohm Causal Interpretation of Quantum Mechanics* (Cambridge University Press, Cambridge, 1993).

[38] R. E. Wyatt, *Quantum Dynamics with Trajectories, Introduction to Quantum Hydrodynamics, Interdisciplinary Applied Mathematics* (Springer, New York, 2005), Vol. 28.

[39] S. W. McDonald and A. N. Kaufman, Phys. Rev. A **37**, 3067 (1988).

[40] K. J. Ebeling, in *Mathematical Physics and Applied Mathematics 7, Contemporary Mathematics 5*, edited by W. P. Mason and R. N. Thurston (Academic, New York, 1984), Vol. 17, p. 233.

[41] T. Ando, Phys. Rev. B **44**, 8017 (1991).

[42] U. Kuhl, Eur. Phys. J. Spec. Top. **145**, 103 (2007).

[43] U. Kuhl, E. Persson, M. Barth, and H.-J. Stöckmann, Eur. Phys. J. B **17**, 253 (2000).